

Isochoric, isobaric, and ultrafast conductivities of aluminum, lithium, and carbon in the warm dense matter regime

M. W. C. Dharma-wardana* and D. D. Klug

National Research Council of Canada, Ottawa, Ontario, Canada K1A 0R6

L. Harbour and Laurent J. Lewis

Département de Physique, Université de Montréal, Montréal, Québec, Canada H3T 1J4

(Received 20 September 2017; revised manuscript received 7 November 2017; published 27 November 2017)

We study the conductivities σ of (i) the equilibrium isochoric state σ_{ic} , (ii) the equilibrium isobaric state σ_{ib} , and also the (iii) nonequilibrium ultrafast matter state σ_{uf} with the ion temperature T_i less than the electron temperature T_e . Aluminum, lithium, and carbon are considered, being increasingly complex warm dense matter systems, with carbon having transient covalent bonds. First-principles calculations, i.e., neutral-pseudoatom (NPA) calculations and density-functional theory (DFT) with molecular-dynamics (MD) simulations, are compared where possible with experimental data to characterize σ_{ic} , σ_{ib} , and σ_{uf} . The NPA σ_{ib} is closest to the available experimental data when compared to results from DFT with MD simulations, where simulations of about 64–125 atoms are typically used. The published conductivities for Li are reviewed and the value at a temperature of 4.5 eV is examined using supporting x-ray Thomson-scattering calculations. A physical picture of the variations of σ with temperature and density applicable to these materials is given. The insensitivity of σ to T_e below 10 eV for carbon, compared to Al and Li, is clarified.

DOI: [10.1103/PhysRevE.96.053206](https://doi.org/10.1103/PhysRevE.96.053206)

I. INTRODUCTION

Short-pulsed lasers as well as shock-wave techniques can probe matter in hitherto experimentally inaccessible regimes of great interest. These provide information needed for understanding normal matter and unusual states of matter, in equilibrium or in transient conditions [1,2]. Similar hot-carrier processes occur in semiconductor nanostructures [3,4]. Such warm dense matter (WDM) systems include not only equilibrium systems where the ion temperature T_i and the electron temperature T_e are equal, but also systems where $T_i \neq T_e$, or highly nonequilibrium systems where the notion of temperature is inapplicable [5]. While the prediction of a quasi-equation-of-state (quasi-EOS) and related static properties for two-temperature ($2T$) systems [6] is satisfactory, the conductivity calculations using standard codes, even for sodium at the melting point, require massive quantum simulations with as many as ~ 1500 atoms and over 56 k points (according to Ref. [7]), whereas even theories of the 1980s evaluated the sodium conductivities successfully via a momentum-relaxation-time (τ_{mr}) approach [8]. This τ_{mr} is also used in Drude fits to the Kubo-Greenwood (KG) formula used with density-functional theory (DFT) and molecular dynamics (MD) methods. The KG formula and its scope are discussed further in the Appendix.

The static electrical conductivities of WDM equilibrium systems (i.e., $T_i = T_e$), as well as $2T$ quasiequilibrium systems, are the object of the present study. We distinguish the isobaric equilibrium conductivity σ_{ib} and the isochoric equilibrium conductivity σ_{ic} from the ultrafast matter (UFM) quasiequilibrium (isochoric) conductivity σ_{uf} . The $2T$ WDM states exist only for times shorter than the electron-ion

equilibration time τ_{ei} and may be accessed using femtosecond probes.

We consider three systems of increasing complexity above the melting point: (a) a simple system, viz., WDM aluminum at density $\rho = 2.7 \text{ g/cm}^3$; (b) WDM lithium at 0.542 g/cm^3 ; and (c) WDM carbon ($2.0\text{--}3.7 \text{ g/cm}^3$) including the low- T covalent-bonding regime. As experimental data are available for the isobaric evolution of Al and Li starting from their nominal normal densities and down to lower densities of the expanded fluid, we calculate σ_{ib} for Al and Li. The ultrafast conductivity σ_{uf} is calculated for all three materials, as σ_{uf} is conveniently accessible via ultrafast laser experiments, though with low accuracy.

The electrons in WDM Li are known to be nonlocal with complex interaction effects. For instance, clustering effects may appear [9] as the density is increased. Warm dense matter carbon is a complex liquid with transient covalent bonding where the C-C bond energy E_{CC} may reach $\sim 8 \text{ eV}$ in dilute gases (see Sec. IV). The three conductivities σ_{ic} , σ_{ib} , and σ_{uf} for Al, Li and C, are calculated via two so-called first-principles methods where, however, both finally use a mean-free-path model to estimate the conductivity. The appellation “first principles” is used in the sense that the use of an exchange-correlation functional based on a well-established model (e.g., the uniform electron gas at finite T) is admitted under such an appellation. Controlled mathematical or physical approximations to handling the Hamiltonian are also allowed. The two methods used are (i) the neutral pseudoatom (NPA) method as formulated by Perrot and Dharma-wardana [6,10–12] together with the Ziman formula and (ii) the DFT-MD and KG approach as available in codes such as VASP [13] and ABINIT [14], enabling us to assess the extent of the agreement among these theoretical methods and the available experiments. The liquid-metal experimental data are still the most accurate data on WDM systems available; they are used where possible to compare with our calculations.

*chandre.dharma-wardana@nrc-cnrc.gc.ca

Accurate experimental data for the isobaric liquid state of Al [15,16] and Li [17] are available and provide a test of the theory. No reliable isobaric carbon data are available; carbon at 3.7–3.9 g/cm³ and 100–175 GPa was studied recently by x-ray Thomson scattering (XRTS) [18]. Hence we evaluate only σ_{ic} and σ_{ib} in this case, for ρ in the range of XRTS experiments and related simulations [19]. The conductivity across a recently proposed phase transition [20] in low-density carbon (~ 1.0 g/cm³) near $T \simeq 7$ eV is not addressed here.

Density-functional theory with MD methods treat hot plasmas as a thermally evolved sequence of frozen solids with a periodic unit cell of N atoms, typically $N \sim 100$, although order-of-magnitude larger systems may be needed [7] for reliable transport calculations. The static conductivity σ is evaluated from the $\omega \rightarrow 0$ limit of the KG $\sigma(\omega)$ using a phenomenological model [e.g., the Drude $\sigma(\omega)$ [7,21] or modified Drude forms [22]]. More discussion of these issues is given in the Appendix. The N -ion DFT-MD model does not allow an easy estimate of single-ion properties, e.g., the mean number of free electrons per ion (\bar{Z}) or ion-ion pair potentials. In the DFT-MD model an approximation to the latter can be obtained by inverting the MD $g(r)$ using MHNC inversion methods [23,24] or using reverse Monte Carlo approaches [19,25]. Reverse Monte Carlo methods as currently used are unable to capture long-range Friedel oscillations in pair potentials. In contrast, the NPA yields the pseudopotentials and pair potentials as a matter of course.

The NPA methods, e.g., that of Perrot and Dharma-wardana, reduce the many-electron, many-ion problem to an effective one-electron, one-ion problem using DFT [10,11,26]. A Kohn-Sham (KS) calculation for a nucleus immersed in the plasma medium provides the bound and free KS states. While bound states remain localized within the Wigner-Seitz sphere of the ion for the regime studied here, the free-electron distribution $n_f(r)$ of each ion resides in a large correlation sphere such that all $g_{ij}(r) \rightarrow 1$ as $r \rightarrow R_c$. We typically use an R_c of ten times the Wigner-Seitz (WS) radius; thus $R_c = 10r_{WS}$, i.e., a volume of some 1000 atoms. Several average-atom models [27,28] have similarities and significant differences among them and with the NPA method. These are reviewed in the Appendix and in Ref. [20]. The NPA method applies for low- T systems even with transient covalent bonding. Hence, we differ from Blenski *et al.* [28], who hold that “... all quantum models seem to give unrealistic description of atoms in plasma at low T and high plasma densities.” However, in reality, the earliest successful applications of the NPA were for solids at $T = 0$. Here we treat very-low- T WDMs, e.g., Al, with $\rho = 2.7$ g/cm³ and $T/E_F < 0.01$, using the NPA, E_F being the Fermi energy, and obtain very good agreement for EOS data [6] and for transport properties, e.g., the electrical conductivity, as shown in detail in this study and in previous studies [29].

The NPA static conductivity is evaluated from the Ziman formula using the NPA pseudopotential $U_{ei}(k)$ and the ion structure factor $S(k)$ [11] generated from the NPA pair potential $V_{ii}(r)$. The latter is used in the hypernetted-chain (HNC) equation or its modified (MHNC) form inclusive of bridge functions, assuming spherical symmetry appropriate to fluids. Hypernetted-chain methods are accurate, fast, and much cheaper than MD methods, which fail to provide small- k information, i.e., less than $\sim 1/L_{bx}$, where L_{bx} is the linear

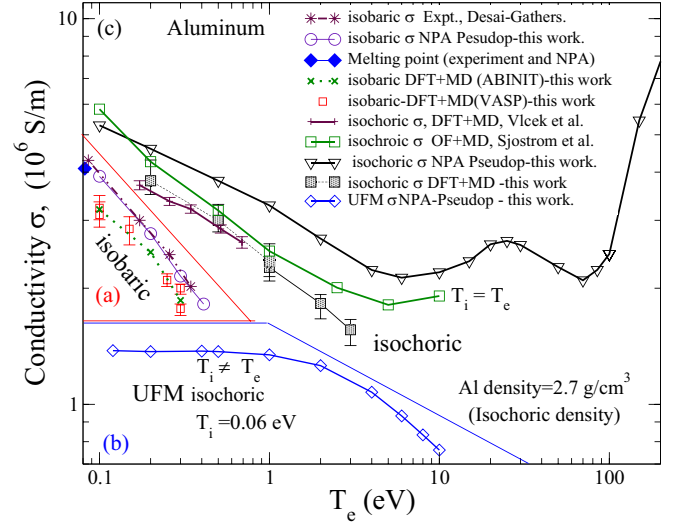


FIG. 1. Static conductivities for Al from experiment and from DFT-MD and NPA calculations. The isobaric conductivity σ_{ib} is at densities $2.37 \geq \rho \geq 1.65$ g/cm³ [cf. triangular region (a)]. The isochoric [σ_{ic} , region (c)] and UFM [σ_{uf} , region (b)] conductivities are for a density of 2.7 g/cm³. Enlarged views of regions (a) and (c) are given in the Appendix. The blue closed diamond gives the conductivity of normal aluminum at its melting point (0.082 eV and 2.375 g/cm³), viz., $\sigma = 4.16 \times 10^6$ S/m from experiment (quoted in Ref. [34]) and $\sigma = 4.09 \times 10^6$ S/m from the NPA calculation.

dimension of the simulation box. The Ziman formula can be derived from the Kubo formula using the force-force correlation function or with the Fermi golden rule [30] and assuming a momentum-relaxation time τ_{mr} . Zubarev’s method can also be used [31] to derive the Ziman formula. Details regarding the conductance formulas and their limitations are given in the Appendix.

II. CONDUCTIVITIES OF WDM ALUMINUM

Surprisingly low static conductivities for UFM aluminum at 2.7 g/cm³, extracted from x-ray-scattering data from the Linac Coherent Light Source (LCLS), have been reported by Sperling *et al.* [32]. Calculations of σ_{ic} using an orbital-free (OF) form of DFT and MD revealed sharp disagreement with the LCLS data [33]. Sperling *et al.* [32] found the conductivity data of Gathers [15] to differ strikingly from the LCLS data and the OF results. In Fig. 4 of Ref. [32], they attempt to present a theoretical σ_{ic} at 2.7 g/cm³ that agrees approximately with the Gathers’ data and to some extent with the LCLS data. The Gathers data are reviewed in the Appendix.

However, in our view, the LCLS, OF, and Gathers σ *should* indeed differ, both in the physics involved and in the actual values, because (i) the Gathers data are for the *isobaric* conductivity σ_{ib} of liquid aluminum from $\rho = 1.7$ to 2.4 g/cm³ [cf. region (a) in Fig. 1], (ii) the orbital-free simulation [33] and the DFT with MD simulations of Vlcek *et al.* [35] are for the *isochoric* equilibrium ($T_e = T_i$) σ_{ic} of Al at $\rho = 2.7$ g/cm³ [region (c) in Fig. 1], and (iii) the LCLS data apply to UFM aluminum σ_{uf} , $T_i \neq T_e$, with the ions frozen at $T_i \simeq T_0$, as proposed in Ref. [36]. The UFM conductivity is shown as region (b) in Fig. 1. The ultrafast conductivity σ_{uf} is essentially

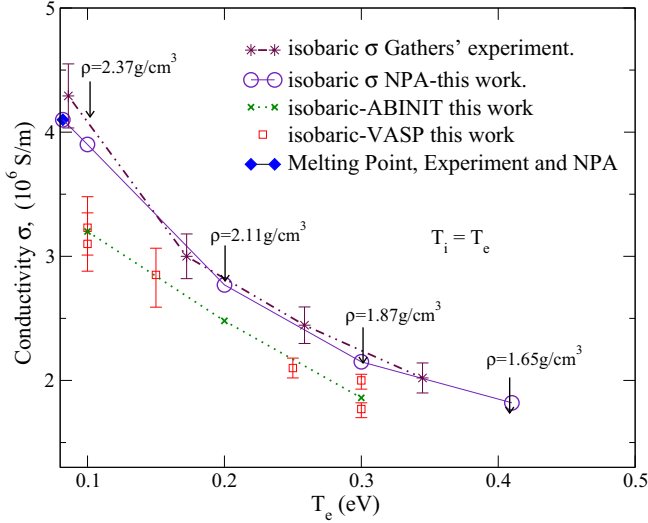


FIG. 2. Isobaric conductivity of aluminum from near its melting point to about 0.4 eV, expanded from Fig. 1 and with linear scales. We compare the NPA calculation, Gathers' experiment, and our DFT with MD results. The experimental σ_{ib} of Al at its melting point (blue closed diamond) [34] $\rho = 2.375$ g/cm³ is displayed and aligns with the NPA calculations for the Gathers data showing agreement between the NPA calculation and two independent experiments.

isochoric, with $T_i \simeq T_0$ at the density ρ_0 . The time scales in UFM experiments are too short for (ρ, T_i) to differ significantly from (ρ_0, T_0) . The evaluation of the ultrafast conductivity σ_{uf} was discussed in detail in Ref. [36] and here we extend our study of UFM conductivities.

A. Isobaric conductivity

In Fig. 1 we globally compare our NPA-Ziman isobaric conductivities for aluminum with the isochoric and UFM conductivities, shown in regions (b) and (c). The three conductivities evolve in characteristic ways as a function of temperature.

The experimental data of Gathers for σ_{ib} are compared with our results in more detail in Fig. 2 and we find *excellent agreement* with our NPA calculation. The DFT-MD calculations using a 108-atom simulation cell are shown in both figures for σ_{ib} and σ_{ic} .

The DFT-MD calculations in this study use the Perdew-Burke-Ernzerhof (PBE) functional [37] in the generalized gradient approximation (GGA), available in VASP and ABINIT. An energy cutoff of 12 hartree was imposed, while a Nosé-Hoover thermostat with a time step of 100 a.u. (2.4188 fs) was used. In all cases the current versions of the codes were implemented and the pseudopotentials proposed therein were used. The projected augmented wave potentials supplied with the code were used in VASP simulations. The finite- T implementation of DFT codes used an occupation-number smearing to simulate the Fermi functions [14]. The highest- k mesh (Monkhorst-Pack grid) tested was $4 \times 4 \times 4$, but the $2 \times 2 \times 2$ mesh was adopted for all our reported calculations. More details on the simulation parameters used, such as occopt, tsmer, etc. (e.g., for ABINIT runs), or equivalent parameters used for VASP runs followed standard usage and are available from the authors.

The DFT-MD-KG results for the conductivity fall below the experimental σ_{ib} or the NPA σ_{ib} , a common trend for the DFT-MD-KG σ_{ic} as well, as discussed further in the Appendix. It should be noted that Gathers gives two isobaric resistivities in columns 4 and 5 of Table II in Ref. [15] and this has caused some confusion; Gathers' results are further discussed in the Appendix, noting that column 5 of [15] is the 'raw data'.

The isochoric conductivity of Al at 0.082 eV (nominal melting point) is $\approx 5 \times 10^6$ S/m; the experimental isobaric conductivity [34] at the melting point is $\sigma_{ib} = 4.1 \times 10^6$ S/m, with a density of 2.375 g/cm³ instead of the room-temperature density of 2.7 g/cm³ due to thermal expansion. The value of 4.08×10^6 S/m obtained from NPA calculations for aluminum at 2.375 g/cm³ is in excellent agreement with experiment. It is shown as a blue closed diamond in Fig. 1. This value drops to 3.8×10^6 S/m if a bridge contribution (MHNC) is not used in calculating the ion-ion structure factor.

B. Isochoric conductivity

The isochoric system, region (c) in Fig. 1, is at $\rho_0 = 2.7$ g/cm³ and $r_{WS} \simeq 2.98$ a.u. ($\hbar = |e| = m_e = 1$) for all $T = T_i = T_e$. The NPA value of σ_{ic} at $T = 0.082$ eV (nominal melting point) is $\approx 5 \times 10^6$ S/m; this is higher than the experimental value usually quoted [34] of $\sigma_{ib} = 4.1 \times 10^6$ S/m as the density of normal aluminum becomes 2.375 g/cm³ instead of 2.7 g/cm³ due to thermal expansion. In region (c) we see the OF conductivity of Ref. [33] going to a minimum at $T \sim 5$ eV and subsequently rise as T increases; the DFT-MD-KG formula becomes increasingly prohibitive at these higher temperatures. The NPA calculations show a first minimum at ~ 6 eV, followed by a maximum at 25 eV and another minimum at ~ 70 eV. These features in the NPA results are due to the concurrent increase in \bar{Z} as well as the competition between different ionization states. This effect, i.e., the conductance minimum or resistivity saturation, occurs when electrons become nondegenerate (i.e., $\mu_e \leq 0$), i.e., when all electrons (not just those near $E_F \sim 12$ eV) begin to conduct.

While we favor this explanation of the minimum in the conductivity and first presented it in our discussion [38] of the Mlischberg experiment, some authors (e.g., More in Ref. [2] and also Faussurier and Blancard [39]) have proposed an explanation in terms of resistivity saturation, as in Mott's theory of minimum conductance in semiconductors. The electron mean-free path $\lambda = \bar{v} \tau_{mr}$, where \bar{v} is the mean electron velocity, is claimed to reduce to the mean interatomic distance at resistivity saturation. However, τ_{mr} evaluated using the Ziman formula is a momentum-relaxation time associated with scattering within the thermal window of the Fermi distribution at the Fermi energy (more accurately, at an energy corresponding to the chemical potential). Since $2k_F$ is of the order of an inverse r_{WS} , it is not surprising that one can connect a length scale related to r_{WS} to λ . However, it does not describe the right physics of the conductivity minimum. Even the simplest form of the Ziman formula already shows the conductivity minimum and it is a single-center scattering formula using a Born approximation within a continuum model; it contains no information on the interatomic distance since one can even set $S(k) = 1$ and obtain the resistivity

saturation. In contrast, the resistivity saturation shown in Fig. 1 for the NPA calculation manifests itself from approximately half the Fermi energy (≈ 6 eV), corresponding to $\bar{Z} = 3$, to about 70 eV, corresponding to a much higher ionization of $\bar{Z} \approx 7$. The increased ionization prevents the chemical potential from becoming rapidly negative and delays the onset of the steep rise in conductivity. These features cannot be explained via a limiting mean-free-path model. In fact, in an isochoric system the interionic distance does not change and one cannot have the complex structure shown in the NPA σ_{ic} in such a model. For $T_e = 6$ eV to about $T = 25$ eV, $\bar{Z} = 3$ for Al and steadily converts to $\bar{Z} = 4$, and then a decline and a rise are accompanied by the conversion of $\bar{Z} = 4$ to $\bar{Z} \approx 7$ by $T \sim 70$ eV.

Figure 1 of Faussurier and Blancard [39] displays the isochoric resistivity for aluminum together with results from Perrot and Dharma-wardana [40]. However, the latter gives the scattering as well as the pseudopotential-based resistivity for aluminum where the mean *electron* density \bar{n} is held constant, not the usual isochoric resistivity where the ion density $\bar{\rho}$ has to be held constant. Electron-isochoric and ion-isochoric conditions are equivalent initially and as long as $\bar{Z} = 3$ for aluminum, but the comparison becomes misleading beyond $T \approx 15$ eV. Figure 1 of Faussurier and Blancard [39] also displays the aluminum isochoric resistivity from Yuan *et al.* [41]. However, as explained in Sec. 3 of the Appendix, both Faussurier and Blancard and Yuan *et al.* use an ion-sphere model that leads to ambiguities in the definition of \bar{Z} and μ_0 , leading to non-DFT features that are absent in the NPA model. Hence their resistivity estimates are not directly comparable to ours. Sufficiently accurate experiments are not yet available at such high temperatures to distinguish between different theories and validate one or the other. Such models should also be tested using cases where accurate experimental data are available (e.g., in the liquid-metal regime).

A further aspect of conductivity calculations is the need to account for multiply ionized species. For $T > E_F/2$, \bar{Z} begins to increase beyond 3 and departs substantially from an integer (e.g., $\bar{Z} = 3.5$ at 20 eV). It is thus clear that a multiple ionization model with several integral values of \bar{Z} (e.g., a mixture of $\bar{Z} = 3$ and $\bar{Z} = 4$) should be used, as implemented by Perrot and Dharma-wardana [11], for lower-density aluminum. The isochoric data σ_{ic} reported in Fig. 1 use the approximation of a single ionic species with a mean \bar{Z} .

C. Ultrafast conductivity

The nature of ultrafast matter and its properties are determined by the initial state of the system. That is, if the initial system were a room temperature solid and if the experiment were performed with minimal delay after the pump pulse of the laser, then the ion subsystem would remain more or less intact. However, the initial state can also be the liquid state and this will lead to different results. Both these cases are studied to compare and contrast the resulting σ_{uf} for Al.

(i) For the case where the initial state is solid (fcc lattice), we assume for simplicity that the ion-subsystem structure factor $S(k)$ can be adequately approximated by its spherical average since aluminum is a cubic crystal. The major Bragg contributions are included in such an approximation. In fact,

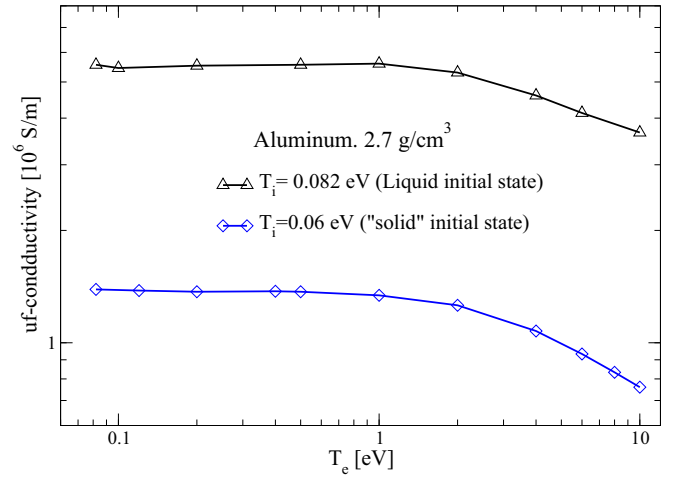


FIG. 3. Ultrafast conductivity of Al at a density of 2.7 g/cm^3 obtained from the NPA-MHNC-Ziman formula for a solid initial state at 0.06 eV (blue curve with diamonds) and liquid initial state (black curve with triangles) just above the melting point 0.082 eV. The top curve was also displayed in Fig. 1 for comparison with σ_{ib} and σ_{ic} .

the spherically averaged $S(k)$ is taken to be the ion-ion $S(k)$ of the supercooled liquid at 0.06 eV as that is the lowest temperature (closest to room temperature) where the Al-Al $S(k)$ could be calculated. The results are in fact insensitive to whether we use the $S(k)$ at 0.06 eV, 0.082 eV (melting point), or 0.1 eV. Furthermore, here we are using the simplest local (*s*-wave) pseudopotential derived from the NPA approach using a radial KS equation. Hence the use of a spherically average $S(k)$ is consistent and probably within the large error bars of current LCLS experiments (see Refs. [32,36]). The NPA σ_{uf} results (Fig. 3) for the case where the initial state is below the melting point (mimicking solid Al) have been compared in detail with the experimental data in Ref. [36]. One notes that the σ_{uf} at $T_e = T_i = 0.6$ eV does not go to the conductivity of solid (crystalline) aluminum, but goes to a lower value, possibly consistent with that of a supercooled liquid. The lower conductivity, compared to the fcc crystal, is qualitatively consistent with the drop in the conductivity from the solid-state room-temperature density (equal to 2.7 g/cm^3) value of $\sigma \approx 41 \times 10^6 \text{ S/m}$ to the liquid-state value at the melting point, $4 \times 10^6 \text{ S/m}$. The drop predicted by the NPA σ_{uf} is larger. Hence this calculation appears to need further improvement for $T < 1.0$ eV, e.g., using the structure factor of the fcc solid and including appropriate band-structure effects.

(ii) The second model we study has molten Al at its nominal melting point (0.082 eV) but at its isochoric density of 2.7 g/cm^3 as the initial state. This mimics the case where the pump pulse had warmed the ion subsystem to some extent. Then we use the $S(k)$ and pseudopotentials evaluated at 0.082 eV (nominal melting point) and regard that they remain unchanged while the electron screening and all properties dependent on the electron subsystem are evaluated at the electron temperature T_e . The resulting σ_{uf} is shown in Fig. 3, together with the case where the initial state was assumed to be a temperature (e.g., the room temperature 0.026 or 0.06 eV) that is below the melting point. The two curves

TABLE I. Gathers' data for Al recalculated from Eqs. (6)–(10) in [15] and also from his fit equation [reproduced as Eq. (A24)] given in the last row of Table 23 of [16].

T (K)	v/v_0 Eq. (A6) [15], Table-II, column 3	ρ (g/cm ³)	R_G ($\mu\Omega$ m) Eq. (A7) [15], Table-II, column 5	$R_{\text{Eq. (9)}} = R_{[16]}$ ($\mu\Omega$ m) Eq. (A8) [15], Table-II, column 4	σ_{ib} 10 ⁶ (S/m) 1/ $R_{\text{Eq. (A8)}}$ 1/ $R_{[16]}$
933	1.12	2.42	0.261	0.233	4.30
1000	1.12	2.41	0.268	0.238	4.20
1500	1.18	2.29	0.331	0.281	3.56
2000	1.24	2.18	0.370	0.324	3.08
2500	1.30	2.08	0.476	0.367	2.73
3000	1.37	1.97	0.560	0.409	2.44
3500	1.44	1.87	0.651	0.451	2.22
4000	1.52	1.77	0.751	0.494	2.03

clearly suggest that the LCLS experiments (see Ref. [36] for details) for Al are more consistent with the initial state (i.e., the state of matter at the peak of the laser pulse) being solid and with no significant premelt.

Currently, no DFT-MD-KG results for σ_{uf} are available for comparison. The usual DFT-MD-KG approach has to be radically modified for DFT-MD-KG calculations of σ_{uf} , given that no ion motion occurs during the lifetime of UFM.

D. Exchange-correlation functionals and the Al conductivity

Using a DFT-MD-KG approach, Witte *et al.* [42] examined the σ for Al at $\rho = 2.7$ g/cm³ and $T = 0.3$ eV computed with the exchange-correlation (XC) functionals of (i) Perdew *et al.* [37] used in their Li work [43] as well, and (ii) Heyd *et al.* [44]. Their results agree with those of Vlček *et al.* [35] for the PBE functional; our DFT-MD calculations also agree well with those of Vlček *et al.* as seen from region (c) in Fig. 1. However, Witte *et al.* propose, from their Fig. 1, that their Heyd-Scuseria-Ernzerhof (HSE) calculation agrees [45] best with the experimental data of Gathers [15]. This is based on a calculation of the conductivity at 0.3 eV only (≈ 3500 K), which is compared with the corresponding entry in Table II, column 4, of Ref. [15], viz., resistivity equal to $0.451 \mu\Omega$ m, i.e., conductivity equal to 2.22×10^6 S/m. However, this datum is given by Gathers for a volume dilation of 1.44 (column 3), i.e., $\rho = 1.875$ g/cm³, and *not* 2.7 g/cm³. Witte *et al.* incorrectly interprets column 4 of Gathers' Table II as providing isochoric conductivities of Al at 2.7 g/cm³. Gathers' tabulation and the several resistivities given are indeed a bit confusing; we reconstruct them in Table I and are further discussed in the appendix.

Columns 4 and 5 of our Table I give two possible results for the isobaric conductivity of aluminum, with column 4 giving the experimental resistivity as a function of the nominal input enthalpy, i.e., raw data. Column 5 of our Table I gives the resistivity where in effect the input enthalpy has been corrected for volume expansion; this is *not* the isochoric resistivity of aluminum, as proposed by Sperling *et al.* [32] and by Witte *et al.* [42] but the isobaric resistivity.

All the resistivities in Gathers' Table II, column 4 (i.e., our Table I, column 5) can be recovered accurately by our parameter-free NPA calculation using the isobaric densities.

Also, the fit formula given in the last row of Table 23 of Gathers' review [16] confirms that Table II, column 4 in Ref. [15] is indeed the final isobaric data at 0.3 GPa. Our NPA calculation at the melting pt. recovers the known isobaric conductivity [34] at 0.082 eV, which is also consistent with the Gathers data.

The HSE functional includes a contribution (e.g., 25%) of the Hartree-Fock exchange functional in it. If there is no band gap at the Fermi energy, the Hartree-Fock self-energy is such that several Fermi-liquid parameters become singular. Hence the use of this functional in WDM studies may lead to uncontrolled or unknown errors. Furthermore, previous studies, e.g., those of Pozzo *et al.* [7] and Kietzmann *et al.* [46], show that the PBE functional successfully predicts conductivities. Those conductivities, if recalculated with the HSE functional, are most likely to be in serious disagreement with the experimental data.

Density-functional theory is a theory that states that the free energy is a functional of the one-body electron density and that the free energy is minimized by just the physical density. It does *not* claim to give, say, the one-electron excitation spectrum or the density of states (DOS). The spectrum and the DOS are those of a fictitious noninteracting electron system at the *interacting density* and moving in the KS potential of the system. The KS potential is not a mean-field approximation to the many-body potential, but a potential that gives the exact physical one-electron density if the XC functional is exact. Hence any claimed agreement between the DFT spectra and physical spectra is not relevant to the quality of the XC functional, except in phenomenological theories that aim to go beyond DFT and recover spectra, DOS, band gaps etc., by including parameters in metafunctionals that are fitted to a wide array of properties. There is however no theoretical basis for the existence of XC functionals that also simultaneously render accurate excitation spectra, DOS, and band gaps in a direct calculation.

Witte *et al.* [42] use their HSE-generated aluminum conductivity (which leads to the incorrect lower conductivity) in further calculations of x-ray-scattering spectra and conclude that strong electron-electron interactions exist in aluminum. In our view, a more standard interpretation will result if a two-temperature aluminum WDM model is invoked, as in our reanalysis [36] of the study of Al by Sperling *et al.* [32].

In our NPA calculations we have used the PDW XC functional derived from the classical-map model of the finite- T homogeneous electron fluid (see Ref. [47]). A comparison of the PDW XC functional with finite- T quantum Monte Carlo results is given in Ref. [48] and shows excellent agreement, especially in the regimes of r_s and T relevant to WDMs. Unlike in the DFT-MD method, which works with a highly inhomogeneous multicenter electron distribution, the NPA works with a single-center electron distribution that is more smooth in comparison and hence the local-density approximation (LDA), adopted here, usually works quite well.

E. Variation of the conductivity as a function of temperature

The evolution with temperature of the conductivity can be understood within the physical picture of electrons near the Fermi energy (chemical potential) undergoing scattering from the ions in a correlated way via the structure factor. However, the scattering is possible within the thermal smearing window $W = f(\vec{k}, T)\{1 - f(\vec{k} + \vec{q}, T)\}$, where $f(k, T)$ is the Fermi occupation factor and $\{1 - f(\vec{k} + \vec{q}, T)\}$ is the available final state for a scattering vector \vec{q} . As can be seen from the Ziman formula, the strength of the scattering in turn involves the $S(k)$ whose peak position relative to the Fermi momentum k_F becomes relevant. The breakdown of the Fermi surface as T/E_F increases leads to a widening of W . These effects are countered to some extent by the increasing ionization that increases the Fermi energy and the degeneracy. However, the decrease of μ^0 with temperature is dominant and at sufficiently high temperatures the chemical potential μ^0 tends to zero and to negative values (we only need to consider μ^0 within a DFT context). The conductivity then becomes that of a classical charged fluid (see Ref. [38]). This is easily understood by noting that μ^0 is of the form [49]

$$\mu^0/E_F = 1 - \frac{\pi^2}{12}(T/E_F)^2 - 0.7103(T/E_F)^4 + \dots \quad (1)$$

When μ^0 becomes sufficiently negative, the Fermi factors simplify to Boltzmann factors and there is no Fermi surface or Fermi statistics to limit the electron scattering; then the conductivity increases with temperature as in Spitzer theory. Hence we conclude that the conductivity minimum (resistivity plateau) in WDM systems occurs in transiting from the metal-like conductivity of (partly or fully) degenerate electrons that *decrease* with temperature to the classical-plasma conductivity of nondegenerate electrons that *increase* with temperature. It is not related to the Mott minimum conductivity.

The differences between σ_{ic} and σ_{uf} , both isochoric, arise because the structure factors $S(k, T_i)$ of the two systems are different, while $U_{ei}(k)$ and the Fermi-surface smearing for them are essentially the same at T_e , with $\bar{Z} \simeq 3$ for Al. The ion structure factors at different temperatures, calculated using the NPA pseudopotential $U_{ei}(k, T_e)$ and used for evaluating σ_{ic} , are shown in Fig. 4(a). The U_{ei} and $S(k)$, and hence σ , are first-principles quantities determined entirely from the NPA-KS calculation. If the initial temperature T_0 at the time of creation of the Al UFM were 0.082 eV (i.e., on the order of the melting point), then the corresponding $S(k, T_0)$ is used in evaluating σ_{uf} at all T_e , together with the $U_{ei}(k, T_e)$. More details of σ_{uf} and a comparison with LCLS data may be found in Ref. [36].

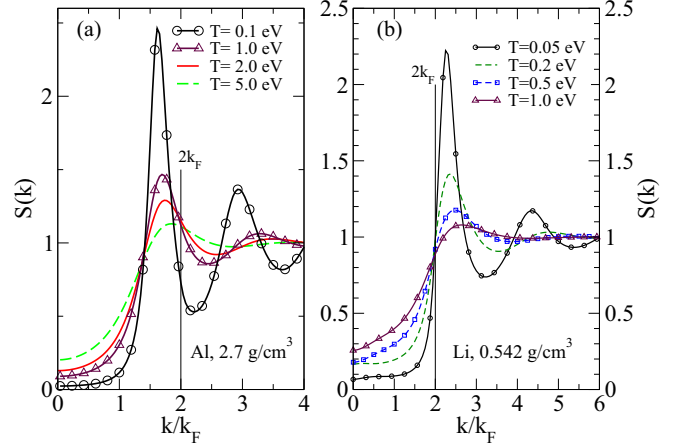


FIG. 4. (a) Static structure factor $S(k)$ of isochoric aluminum WDM at different temperatures; $S(k)$ at $2k_F$ changes by 65% from $T = 0.1$ to $T = 5$ eV. In ultrafast aluminum $S(k)$ remains fixed at the initial temperature, even when T_e changes. (b) Evolution of $S(k)$ for isochoric Li at 0.542 g/cm^3 as a function of temperature. As T increases, the peak broadens and shifts away from $2k_F$.

The isobaric system differs from the isochoric and ultrafast systems due to volume expansion. Hence the $S(k)$ and the U_{ei} are calculated at each expanded density.

Degenerate electrons ($T_e/E_F < 1$) scatter from one edge (e.g., $-k_F$) of the Fermi surface to the opposite edge (k_F), with a momentum change $k \simeq 2k_F$, and their scattering contribution essentially determines σ . Thus the position of $2k_F$ with respect to the main peak of $S(k)$ and its changes with T_e explain the T_e dependence of $\sigma(T_e)$. For aluminum at $\rho = 2.7 \text{ g/cm}^3$, $2k_F$ lies on the high- k side of the main peak, and as $T_i = T_e$ increases, the peak broadens into the $2k_F$ region [see Fig. 4(a)], resulting in increased s . In the isochoric UFM case both T_i and $S(k)$ do not change, but as T_e increases the window of scattering $f(k)[1 - f(k')]$, where \vec{k}' is the final state, becomes larger and σ_{uf} decreases.

As Fig. 4 is burdened with many plots, we have given the comparison of Al and Li ion-ion pair-distribution functions obtained from DFT-MD and NPA-MHNC simulations separately. However, the good agreement of NPA $g(r)$ and $S(k)$ with DFT-MD data, or experimental $S(k)$, is routinely found for compressions of 0.5 to twice the normal density. Such agreement with DFT-MD simulations is seen in, e.g., Fig. 8 of Ref. [6] for Li and in Figs. 1 and 3 of Ref. [46]. We give a comparison of the NPA-MHNC equation generated $g(r)$ for Al and Li at 2.7 and 0.542 g/cm^3 , respectively, at 1 eV where they are partially degenerate WDMs, in Fig. 5. The details for the DFT-MD simulations are as described in Sec. II A. The NPA calculation is with the PDW local-density XC functional [47] for the electrons, as explained in Sec. II D, while the HNC-bridge functional was used for the classical correlations.

The excellent agreement between the NPA σ_{ib} and the Gathers aluminum data for σ_{ib} (see Fig. 2) confirms the accuracy of NPA pseudopotentials U_{ei} , structure factors, and XC functionals used and enhances our confidence in the NPA predictions for σ_{ic} . Conductivity experiments at other density ranges had also been found to be in good agreement with NPA calculations [29] and with the DFT-MD calculations of

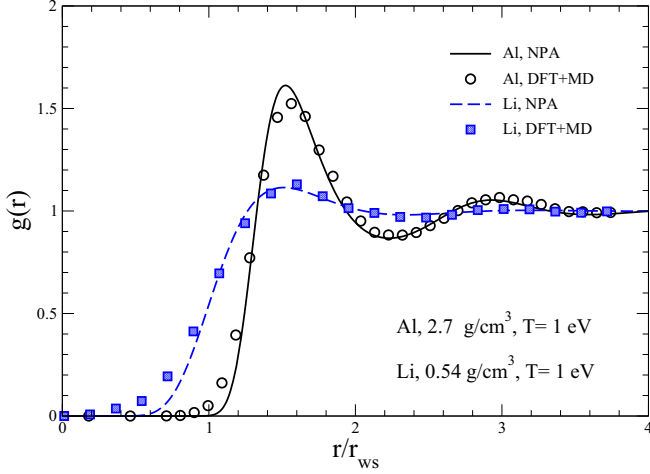


FIG. 5. The NPA-MHNC $g(r)$ of isochoric Al at 1 eV, $\rho = 2.70 \text{ g/cm}^3$, and $r_{\text{WS}} \simeq 3.0$ and isochoric Li at 1 eV, $\rho = 0.542 \text{ g/cm}^3$, and $r_{\text{WS}} \simeq 3.3$ compared with the DFT-MD $g(r)$ obtained using ABINIT and 108 atoms in the simulation. At 1 eV, $T/E_F \sim 0.1$ and 0.2 for Al and Li, respectively, which correspond to partially degenerate WDM systems.

Dejarlais *et al.* [50]. Furthermore, the NPA approach becomes more reliable at higher temperatures ($T/E_F > 1$) while the DFT-MD methods rapidly become impractical due to the large number of electronic states that are needed in the calculation due to the spread in the Fermi distribution. At lower T , ion-ion correlations and interactions become important and the DFT-MD method treats them well. However, at low T , the higher conductivities imply longer mean free paths and the need for simulation cells with larger L_{bx} [51]. Good DFT-MD-KG results, when available, provide benchmarks for calibrating other methods.

III. CONDUCTIVITIES OF WDM LITHIUM

The three conductivities σ_{ic} , σ_{ib} , and σ_{uf} for Li are shown in Fig. 6. The isobaric data are in the triangular region. All calculations except that due to Witte *et al.* shown here are from the NPA-MHNC-Ziman formula. For $T/E_F > 0.3$ the bridge corrections become negligible and the MHNC equation becomes equivalent to the HNC equation.

The NPA isochoric conductivities σ_{ic} at a density of $\rho = 0.542 \text{ g/cm}^3$, i.e., $r_{\text{WS}} = 3.25 \text{ a.u.}$, are given for a range of T , while one value at $\rho = 0.6 \text{ g/cm}^3$ and $T_e = T_i = 4.5 \text{ eV}$ is also given. This is for conditions reported by Witte *et al.* [43]. The experimental isobaric data from Oak Ridge National Laboratory [17] for σ_{ib} (0.5 g/cm^3 at 0.05 eV to 0.4 g/cm^3 at 0.1378 eV), as well as the NPA σ_{ib} , are also shown. Unlike aluminum, Li is a low-electron-density material with $\bar{Z} = 1$. Hence its $E_F \sim 5 \text{ eV}$ is small compared to that of aluminum. For Li, $2k_F$ lies on the low- k side of the main peak, as can be seen in Fig. 4(b). The UFM conductivity σ_{uf} remains higher than the σ_{ic} and its temperature dependence can be understood, as discussed in Sec. II E, by the varying position of k_F with respect to $S(k)$ as T_e varies.

The agreement between the NPA σ_{ib} and the Oak Ridge National Laboratory data for isobaric Li is moderate. The NPA

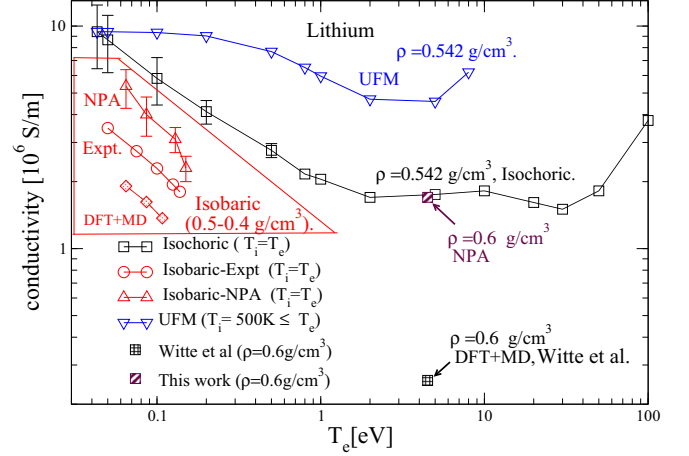


FIG. 6. Isochoric (σ_{ic}), isobaric (σ_{ib}), and ultrafast (σ_{uf}) conductivities of Li at a density of 0.542 g/cm^3 obtained from the NPA-MHNC-Ziman formula. Isochoric experimental conductivities σ_{ib} are for $0.5 \geq \rho \geq 0.4 \text{ g/cm}^3$. The DFT-MD-KG σ_{ic} value of Witte *et al.* at 0.6 g/cm^3 [43], and the corresponding NPA-MHNC-Ziman value for σ_{ic} are also shown.

Li pseudopotential is the simplest local (s -wave) form and corrections (e.g., for the modified DOS) have not been used. In Fig. 7 we have attempted to compare the Oak Ridge National Laboratory experimental data for liquid lithium with the DFT-MD-KG calculations of Kietzmann *et al.* [46]. We use their calculations as a function of density for 600 and 1500 K. The Kietzmann *et al.* calculation at 2000 K is also shown in Fig. 7, but since the boiling point of lithium under isobaric conditions is $\simeq 1600 \text{ K}$, their calculation at 2000 K cannot be justifiably used to estimate a value for 1500 K from the data of Kietzmann *et al.*, which also include the two points at 600 and 1000 K.

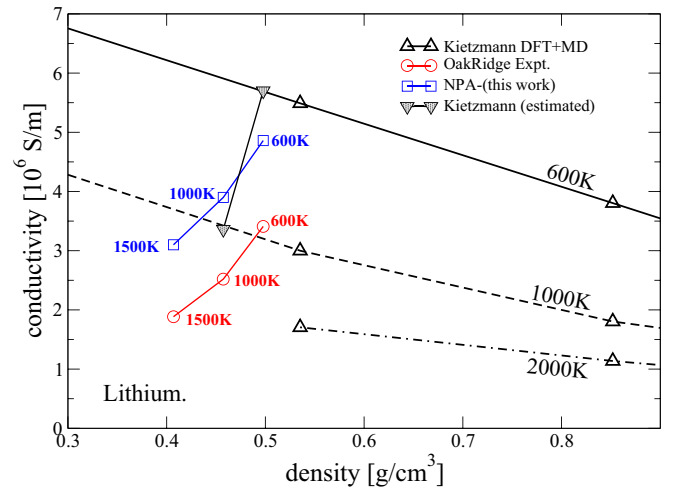


FIG. 7. Oak Ridge National Laboratory experimental data compared with the NPA-MHNC-Ziman results and the DFT-MD-KG conductivity of Kietzmann *et al.* [46] using the VASP code. Their 600 and 1000 K results have been slightly extrapolated to the low-density region covered by the experiments. The curve at 2000 K given by Kietzmann *et al.* is above the boiling point of Li and is not representative of the behavior of Li at 1500 K.

Nevertheless, their results are consistent with the observed trend and agree with our NPA results to the same extent as with the Oak Ridge National Laboratory data.

Disconcertingly, the NPA-Ziman formula and the DFT-MD σ_{ic} for $\rho = 0.6 \text{ g/cm}^3$ and $T = 4.5 \text{ eV}$ reported by Witte *et al.* [43] using a 64-atom simulation cell disagree by a factor of 5. However, the NPA-XRTS calculations for Li (see the Appendix) agree very well with the DFT-XRTS experiment of Witte *et al.* Furthermore, we had already shown that the pair-distribution functions from the NPA calculations for Li for the density range of interest are in good agreement with the simulations of Kietzmann *et al.* (see Ref. [6]). However, at $T = 4.5 \text{ eV}$, $\mu = 0.035 \text{ a.u.}$, i.e., the plasma is nearly classical. Hence small- k scattering becomes important in determining σ . A simulation cell of length $a = 20.26 \text{ a.u.}$ holds for 64 atoms. The smallest momentum accessible is $\pi/a = 0.16 \text{ (a.u.)}^{-1}$ and fails to capture the smaller- k contributions to σ . These could cause the observed differences between the NPA and DFT-MD-KG results.

IV. CONDUCTIVITIES OF WDM CARBON

Solid carbon is covalently bonded, with strong sp^3, sp^2, sp bonding (with a bond energy of $\sim 8 \text{ eV}$) being possible, since a single covalent bond has an energy of about 4 eV [20,52]. Hence efforts to create potentials extending to several neighbors, conjugation, torsional effects, etc., have generated complex semiempirical bond-order potentials parametrized to fit data bases but without any T dependence. Transient C-C bonds occur in liquid-WDM carbon. Normal-density liquid C near its melting point is a good Fermi liquid with four free electrons ($\bar{Z} = 4$) per carbon. Unlike in bond order potentials where the electron fluid is subsumed, we explicitly retain a two-component (ions and electrons) description and obtain simple, successful NPA potentials for carbonlike fluids. An early comparison of Car-Parrinello calculations for carbon with the NPA method was reported by Dharma-wardana and Perrot [53]. The NPA method successfully predicts the $S(k)$ and $g(r)$, inclusive of prepeaks due to C-C bonding [20] as also obtained from DFT-MD simulations of WDM carbon [18,19]. The DFT and path-integral Monte Carlo $g(r)$ [54] also agree closely with NPA results [20].

No experimental σ_{ib} are available for carbon; hence we calculate only σ_{ic} and σ_{uf} to display the remarkable difference in the conductivities of complex WDMs with (transient) covalent bonding, compared to simpler WDMs like Al and Li. Figure 8(a) displays σ_{ic} and σ_{uf} for isochoric carbon at 3.7 g/cm^3 . Here E_F is $\sim 30 \text{ eV}$ (for $\bar{Z} = 4$) and the WDM behaves as a simple metal, with σ dropping as T increases and then increasing at higher T_e when μ_e becomes negative. The conductivity (for $T \leq 0.5E_F$) is determined mainly by the value of $S(k)$ at $2k_F$, shown in Fig. 8(b). This is set by the C-C peak in $S(k)$, which is relatively insensitive to T , and hence σ is also insensitive to temperature (compared to WDM Al or Li) in this regime. The insensitivity of $S(k = 2k_F)$ to temperature also leads to the strikingly different behavior of the ultrafast conductivity for liquid carbon as compared to σ_{uf} and σ_{ic} of WDM Al or Li. In WDM carbon the ultrafast and isochoric conductivities are very close in magnitude.

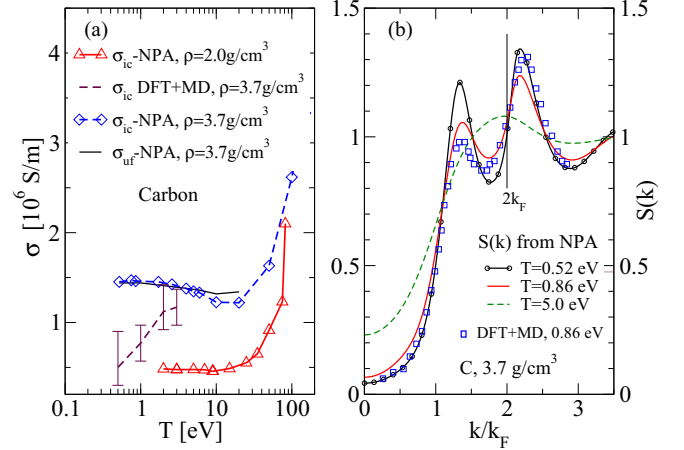


FIG. 8. (a) Isochoric conductivity σ_{ic} and ultrafast conductivity σ_{uf} for carbon at $\rho = 3.7 \text{ g/cm}^3$ from the NPA and DFT-MD methods [18] and isochoric conductivity from the NPA method for $\rho = 2.0 \text{ g/cm}^3$. (b) Ion-ion $S(k)$ for several temperatures from the NPA method; note the nearly constant value of $S(k)$ at $2k_F$ (indicated by a vertical line).

The DFT-MD σ_{ic} values for 3.7 g/cm^3 differ from the NPA method at low- T where strong-covalent bonds dominate. The $N \sim 100$ atom DFT-MD simulations may be seriously inadequate due to such C-C bond formation. The NPA method itself deals only in a spherically averaged way with the covalent bonding. That approximation is probably sufficient for static conductivities if the bonding is truly transient. In any case, accurate experimental σ_{ib} data for liquid carbon are badly needed to test theoretical models.

V. CONCLUSION

Although it is not necessary to distinguish between isochoric and isobaric conductivities, as the specification of the density and temperature is sufficient, such a distinction is useful in comparing experiment and theory. The temperature variations of the three conductivities have distinct features. The ultrafast conductivity is indeed a physically distinct property as the ion subsystem remains unchanged while only the electron subsystem is changed during the short-time delay between the pump pulse and the probe pulse. Thus it is useful to distinguish isochoric, isobaric, and ultrafast conductivities of WDM systems, as illustrated using Al, Li, and C. The NPA σ_{ib} are in excellent agreement with the aluminum experimental data of Gathers [15], while the DFT-MD-KG calculations with 108-atom simulations estimate a lower conductivity. The NPA results are in moderate agreement with the Oak Ridge National Laboratory σ_{ib} for Li, as is also the case with DFT-MD-KG calculations. The carbon σ_{ic} and σ_{uf} from NPA calculations have a striking behavior in the regime of (normal) densities studied here and differ from Al and Li. This is attributed to the effect of transient C-C bonds that are included in the NPA calculations within an average description via effective pair potentials.

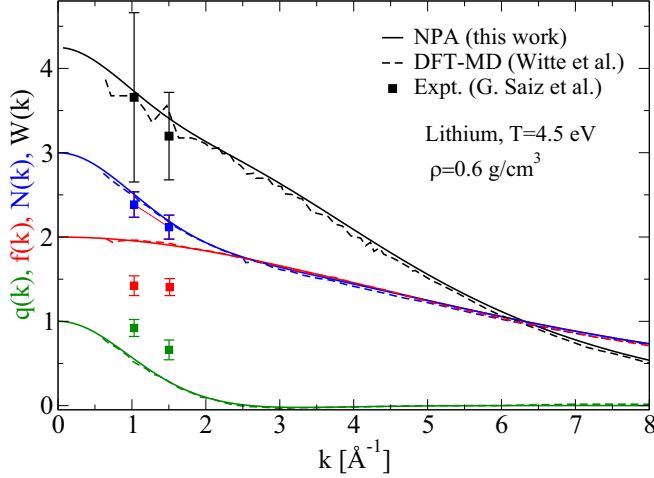


FIG. 9. Quantities relevant to XRTS calculated using the NPA-HNC method (this work) and the DFT-MD method (Ref. [43]) for lithium. Values for k smaller than about 0.6 \AA^{-1} are not available from the DFT-MD simulation due to the finite size of the DFT simulation cell. Here $q(k)$ is the Fourier transform of the free-electron density at the Li ion in the plasma, $f(k)$ is the bound-electron form factor, and $N(k) = f(k) + q(k)$. The ion feature $W(k) = N(k)^2 S(k)$ involves the ion-ion structure factor $S(k)$. Experimental points are from Saiz *et al.* cited in the work of Witte *et al.* [43], Fig. 8.

APPENDIX

This Appendix addresses the following topics: NPA calculation of the XRTS ion feature $W(q)$ for comparison with the DFT-MD calculations of Witte *et al.* [43], where the excellent agreement is in clear contrast to the disagreement for the conductivity datum for Li reported by Witte *et al.*; details of the NPA model and how it differs from other average-atom models; the Ziman formula for the conductivity using the NPA pseudopotential and the ion-ion $S(k)$; KG calculations for Al, Li, and C; Drude fits to the conductivity of Al and Li; and review of the aluminum σ_{ib} and σ_{ic} , the experiment of Gathers, and the disagreement with the conductivity of Al reported in Fig. 1 of Ref. [42] by Witte *et al.* using the HSE XC functional.

1. X-ray Thomson scattering calculation for Li at density $\rho = 0.6 \text{ g/cm}^3$ and temperature $T = 4.5 \text{ eV}$

The calculation of XRTS of WDM using the NPA method has been described in detail in Ref. [55]. The XRTS ion feature $W(k)$ for Li at $T = 4.5 \text{ eV}$ and $\rho = 0.6 \text{ g/cm}^3$ has been calculated (see Fig. 9) to compare our NPA results with the results from the DFT-MD simulations by Witte *et al.* (Ref. [43], Fig. 8). This establishes the excellent agreement with the electronic structure part of the NPA calculation and the ionic part $S_{ii}(k)$ resulting from the DFT-MD calculations, *irrespective* of the XC functional used, viz., PBE GGA by Witte *et al.* and the PDW LDA in NPA calculations. It also implies that the DFT $S(k)$ and the NPA-MHNC $S(k)$ are in agreement.

The mean ionization \bar{Z} for Li in the NPA calculation is unity, as also used by Witte *et al.* They calculate the quantities $q(k)$, $f(k)$, $N(k)$, and $W(k) = N(k)^2 S(k)$. The quantity $q(k)$ is the screening cloud, i.e., the Fourier transform of the free-

electron density at the Li ion in the plasma, while $f(k)$ is the bound-electron form factor and $N(k) = f(k) + q(k)$. Finally, $W(k) = N(k)^2 S(k)$ is known as the ion feature. It involves the ion-ion structure factor $S(k)$.

The excellent accord between our XRTS calculation and that of Witte *et al.* establishes that our $S(k)$, electron charge distributions, and potentials $U_{ei}(k)$ and $V_{ii}(k)$ are fully consistent with the structure data and electronic properties coming from DFT-MD simulations. The $S(k)$ and $U_{ei}(k)$ are the critical inputs to the Ziman formula for σ_0 . Nevertheless, our estimate of the conductivity disagrees strongly with the Kubo-Greenwood estimate of Witte *et al.* Given the relatively good agreement that we found with the Oak Ridge National Laboratory experimental data, as well as with the Kietzmann *et al.* data (see Fig. 7), this disagreement is *a priori* quite surprising; one possible contributory factor (see Sec. 7) may be the use of a small 64-atom DFT-MD simulation cell. The conductivity estimate by Witte *et al.* for $T = 0.3 \text{ eV}$ at 2.7 g/cm^3 is also problematic and it is taken up below, in our discussion of Gathers' results for aluminum.

2. Details of the NPA model and \bar{Z}

The NPA model used here [11,12] has been described in many articles; we summarize it again here for the convenience of the reader, as it should not be assumed that it is equivalent to various currently available ion-sphere (IS) average-atom (AA) models such as PURGATORIO [56] used in many laboratories. While these models are closely related, they invoke simplifications that are outside DFT. The NPA model is a rigorous DFT model based on the variational property of the grand potential $\Omega([n],[\rho])$ as a functional of *both* one-body densities $n(r)$ and $\rho(r)$, directly leading to two coupled KS equations where the unknown quantities are the XC functional for the electrons and the ion-correlation functional for the ions [57]. Approximations arise in modeling those functionals and decoupling the two KS equations [11,30] for simplified numerical work.

The NPA model assumes spherical symmetry for fluid phases and calculates the KS states of a nucleus of charge Z immersed in an electron gas of input density \bar{n} . The ion distribution $\rho(r) = \bar{\rho}g(r)$ is approximated by a neutralizing uniform positive background containing a cavity of radius r_{WS} , with the nucleus at the origin. The Wigner-Seitz (WS) radius r_{WS} is that of the ion-density $\bar{\rho}$, i.e., $r_{WS} = \{3/4\pi\bar{\rho}\}^{1/3}$. The effect of the cavity is subtracted from the final result whereby the density response of a uniform electron gas to the nucleus is obtained. The validity of this approach has been established in previous work and reviewed in Ref. [10]. The solution of the KS equation extends up to $R_c = 10r_{WS}$, defining a correlation sphere (CS) large enough for all electronic and ionic correlations with the central nucleus to have gone to zero. The KS equations produce two groups of energy states, viz., negative and positive with respect to the energy zero at $r \rightarrow \infty$ outside the CS. That is, a Chihara decomposition automatically arises. States in one group decay exponentially to zero as $r \rightarrow R_c$ and in fact become negligible already for $r \rightarrow r_{WS}$ in the case of low- Z elements. These states, fully contained within the WS sphere, are deemed bound states and allow one to define a mean ionization per ion $Z_b = Z - n_b$,

where n_b is the total number of electrons in the bound states and Z is the nuclear charge:

$$Z_b = Z - n_b, \quad n_b = \sum_{nl} 2(2l+1) \int d\vec{r} f_{nl} |\phi_{nl}(r)|^2. \quad (\text{A1})$$

Here $f_{nl} = 1/\{1 + \exp(x_{nl})\}$ and $x_{nl} = \{\epsilon_{nl} - \mu_0\}/T$ is the Fermi factor for the KS state ϕ_{nl} with energy ϵ_{nl} . The noninteracting electron chemical potential μ_0 is used here. Furthermore, there are plane-wave-like phase-shifted KS states that extend through the whole correlation sphere. These are continuum states and their electron population is the free-electron distribution $n_f(r)$. The nucleus Z , the bound electrons n_b , the cavity with a charge $Z_c = (4\pi\bar{n}/3)r_{\text{WS}}^3$, and the free electrons form a neutral object and hence it is a weak scatterer called the neutral pseudoatom. The Friedel sum Z_F of the phase shifts of the continuum states and the cavity charge Z_c add up to zero when the KS equations are solved self-consistently. Thus

$$Z_c = Z_F = \frac{2}{\pi T} \int_0^\infty k f_k (1 - f_k) \sum_l (2l+1) \delta_l(k) dk. \quad (\text{A2})$$

Here $f_k = f_{kl}$ is the Fermi occupation factor for the k, l state with energy $\epsilon = k^2/2$. Full self-consistency requires that

$$Z_b = Z_c = Z_F, \quad \bar{n} = \bar{Z}\bar{\rho}. \quad (\text{A3})$$

Hence, given an input mean free-electron density \bar{n} , the WS radius (equivalently $\bar{\rho}$) is iteratively adjusted until self-consistency is obtained, i.e., Eq. (A3) is satisfied to a chosen precision. The mean ionization $\bar{\rho}$ is thus seen to be the Lagrange multiplier ensuring charge neutrality, as discussed in Ref. [26]. The $\bar{\rho}$ resulting from the input \bar{n} may not be the required physical ion density and hence several values of \bar{n} and the corresponding $\bar{\rho}$ are determined to obtain the actual \bar{n} that corresponds to the required experimental ion density $\bar{\rho}$. This process produces a unique value of \bar{Z} and the problem of having several different estimates of \bar{Z} , as found in IS-AA models [27,56], does not arise here. The agreement among Z_F , Z_c , and Z_b is essential to the convergence of the NPA-KS equations. It is sensitive to the exchange-correlation functional $F_{\text{XC}}(T)$ and to the proper handling of self-interaction (SI) corrections, whenever \bar{Z} is close to a half-integer. Using a valid \bar{Z} is essential to obtaining good conductivities.

We emphasize that a key difference between IS models and the NPA method is that the free electrons are not confined to the Wigner-Seitz sphere, but move in all of space as approximated by the correlation sphere. These differences are discussed in Sec. 3.

In this study we use the local-density approximation to the finite- T XC functional as parametrized by Perrot and Dharma-wardana [47]. This simplest implementation (in the LDA) is a useful reference step needed before more elaborate implementations (involving SI, nonlocality, etc., in the XC functionals) are used.

Since \bar{Z} is the free-electron density per ion, it can develop discontinuities whenever the ionization state of the element under study changes due to, e.g., increase of T or compression. This is analogous to the formation or disappearance of band gaps in solids. In fact, if the NPA model is treated with periodic boundary conditions, as for a solid with one atom in the unit

cell, then the discontinuity in Z appears as the problem of correctly treating the formation of a gap in the DOS at the Fermi energy. A proper evaluation of such features in the DOS and band gaps is difficult in DFT as this is a theory of the total energy as a functional of the one-body density, *not* a theory of individual energy levels. Physical one-electron states are given by the Dyson equation. Thus band-structure calculations inclusive of GW corrections are used in solids to obtain realistic band gaps and excitation energies. In dealing with discontinuities in \bar{Z} , a similar procedure is needed [58], including the use of SI corrections and XC functionals that include electron-ion correlation corrections, i.e., $F_{ei}(n, \rho)$ [57,59].

Some authors have claimed that \bar{Z} “does not correspond to any well-defined observable in the sense of quantum mechanics” [60], i.e., that there is no quantum operator corresponding to \bar{Z} . This view is incorrect as quantities like the temperature T , the chemical potential μ , and the mean ionization \bar{Z} are quantities in quantum *statistical* physics. There may be no operator for them in simple $T = 0$ quantum theories (e.g., not coupled to a heat bath). In most formulations of quantum statistical physics these appear as Lagrange multipliers related to the conservation of the energy, particle number, and charge neutrality. They can be incorporated as operators in more advanced field-theoretic formulations of statistical physics (e.g., as in the thermofield dynamics of Umezawa). Some of these broader issues are discussed in Chap. 8 of Ref. [61].

Finally, it is noted that the mean number of electrons per ion, viz., \bar{Z} , in, e.g., gas-discharge plasmas, is routinely measured using Langmuir probes or derived from optical measurements of various properties including the conductivity and the XRTS profile [62] for WDM plasmas. Hence \bar{Z} is a well-established *measurable* property.

3. Some differences between the NPA model and typical average-atom models

Conductivity calculations using the PURGATORIO model for isobaric aluminum are unavailable for comparison with experimental data. Comparison is also problematic due to the lack of an unequivocal value for the mean ionization \bar{Z} in IS-AA models [56]. We list several differences with the NPA model that particularly affect conductivity calculations.

(i) Most average-atom models are based on the IS-AA model where the free-electron pileup around the nucleus is strictly confined to the Wigner-Seitz sphere

$$\bar{Z} = 4\pi \int_0^{R_{\text{WS}}} \Delta n_f(r) r^2 dr. \quad (\text{A4})$$

This condition was used in Salpeter’s early IS model, in the INFERNO model of Lieberman, and in codes like PURGATORIO [56] derived from it, to determine an electron chemical potential μ_{WS}^0 . It is also used by Yuan *et al.* [41], Faussurier and Blancard [39], Starrett and Saumon [63], and in other AA codes discussed by Murillo *et al.* [27]. However, μ_{WS}^0 is not identical to the noninteracting μ_0 because it includes a confining potential applied to the free-electron density $n_f(r)$ constraining the electrons to the IS. As it is applied via a boundary condition, it is a nonlocal potential. The KS XC potential is also a nonlocal potential and hence the use of Eq. (A4) contaminates the XC potential. On the other hand,

DFT is based on mapping the interacting electrons to a system of *noninteracting electrons* whose chemical potential is rigorously μ_0 , as used in the NPA model that we employ. In the NPA model we use a CS with a large radius R_c ,

$$\bar{Z} = \pi \int_0^{R_c} \Delta n_f(r) r^2 dr. \quad (\text{A5})$$

The upper limit of the integral is $R_c \approx 10r_{\text{WS}}$ and defines a sphere large enough for all correlations with the central ion to have died down at the surface of the sphere. This enables the use of the noninteracting chemical potential in the NPA model, as needed in DFT, since all equations use the large- r limit beyond the CS radius as the reference state.

The constraint placed by Eq. (A4) is clearly invalid at low temperatures where the de Broglie wavelength of the electrons, being proportional to $1/\sqrt{T}$, exceeds r_{WS} at sufficiently low T . Hence such AA models become invalid at low temperatures and are not true DFT models. In contrast, the first successful applications of the NPA were to $T = 0$ solids.

(ii) The use of the constraint placed by Eq. (A4) in AA models has far-reaching consequences as it prevents the possibility of providing a unique definition of the mean ionization, as emphasized by Stern *et al.* [56] in regard to the INFERNO code. In fact, even at high T , there are several definitions of \bar{Z} that differ and hence the estimates of the electrical conductivity are not unambiguous. This is not the case in the NPA model. The problem of discontinuities in \bar{Z} and the band-gap problem in DFT were already discussed in the preceding section.

(iii) The IS-AA models do not satisfy a Friedel sum rule for \bar{Z} , while the f -sum rule is also constrained by the condition imposed by Eq. (A4).

(iv) As the electrons are confined to the WS sphere in IS-AA models, they cannot display prepeaks due to transient covalent bonding as found in liquid carbon, hydrogen, and other low- Z WDMs. This was confirmed by Starrett *et al.* [64] for carbon for their AA model. The bonding occurs by an enhanced electron density in the interionic region between two WS spheres and this is not allowed in IS models. In contrast, the NPA model shows prepeaks in $g_{ii}(r)$ corresponding to transient C-C bonding in liquid carbon and produces a pair potential with a minimum corresponding to the C-C covalent bond distance at sufficiently low T [20]. Neutral pseudoatom calculations for hydrogen show H-H bonding prepeaks in $g(r)$ in the appropriate temperature and density regimes [65].

4. Pseudopotentials and pair potentials from the NPA model

The KS calculation for the electron states for the NPA model in a fluid involves solving a simple radial equation. The continuum states $\phi_{k,l}(r)$ and $\epsilon_k = k^2/2$, with occupation numbers $f_{kl} = f_k$, are evaluated to a sufficiently large energy cutoff and for an appropriate number of l states (typically 9 to 39 were found sufficient for the calculations presented here). The very-high- k contributions are included by a Thomas-Fermi correction. This leads to an evaluation of the free-electron density $n_f(r)$ and the free-electron density pileup $\Delta n'(r) = n_f(r) - \bar{n}$. A part of this pileup is due to the presence of the cavity potential. This contribution $m(r)$ is evaluated using its linear response to the electron gas of density \bar{n} using

the interacting electron response $\chi(q, T_e)$. The cavity-corrected free-electron pileup $\Delta n_f(r) = \Delta n'(r) - m(r)$ is used in constructing the electron-ion pseudopotential as well as the ion-ion pair potential $V_{ii}(r)$ according to the following equations (in hartree atomic units) given for Fourier-transformed quantities:

$$U_{ei}(k) = \Delta n_f(k) / \chi(k, T_e), \quad (\text{A6})$$

$$\chi(k, T_e) = \frac{\chi_0(k, T_e)}{1 - V_k(1 - G_k)\chi_0(k, T_e)}, \quad (\text{A7})$$

$$G_k = (1 - \kappa_0/\kappa)(k/k_{\text{TF}}), \quad V_k = 4\pi/k^2, \quad (\text{A8})$$

$$k_{\text{TF}} = \{4/\pi\alpha r_s\}^{1/2}, \quad \alpha = (4/9\pi)^{1/3}, \quad (\text{A9})$$

$$V_{ii}(k) = Z^2 V_k + |U_{ei}(k)|^2 \chi_{ee}(k, T_e). \quad (\text{A10})$$

Here χ_0 is the finite- T Lindhard function, V_k is the bare Coulomb potential, and G_k is a local-field correction (LFC). The finite- T compressibility sum rule for electrons is satisfied since κ_0 and κ are the noninteracting and interacting electron compressibilities, respectively, with κ matched to the $F_{\text{XC}}(T)$ used in the KS calculation. In Eq. (A9), k_{TF} appearing in the LFC is the Thomas-Fermi wave vector. We use a G_k evaluated at $k \rightarrow 0$ for all k instead of the more general k -dependent form [e.g., Eq. (50) in Ref. [47]] since the k dispersion in G_k has a negligible effect for the WDMs of this study. Steps towards a theory using self-interaction corrections in the F_{XC} , a modified electron DOS, self-energy corrections, etc., have also been given [58,59]. In this study we use the above equations and only in the LDA.

5. Calculation of the ion-ion structure factor

The ion-ion structure factor $S(k)$ is also a first-principles quantity as it is calculated using the ion-ion pair potential, Eq. (A10) given above. For simple fluids like aluminum we use the MHNC equation

$$g(r) = \exp\{-\beta V_{ii}(r) + h(r) - c(r) + B(r)\}, \quad (\text{A11})$$

$$h(r) = c(r) + \bar{\rho} \int d\vec{r}_1 h(\vec{r} - \vec{r}_1) c(\vec{r}_1), \quad (\text{A12})$$

$$h(r) = g(r) - 1. \quad (\text{A13})$$

Here $c(r)$ is the direct correlation function. Thermodynamic consistency (e.g., the virial pressure being equal to the thermodynamic pressure) is obtained by using the Lado-Foiles-Ashcroft (LFA) criterion (based on the Gibbs-Bogoliubov bound for the free energy) for determining $B(r)$ using the hard-sphere model bridge function [66]. That is, the hard-sphere packing fraction η is selected according to an energy minimization that satisfies the LFA criterion. The iterative solution of the MHNC equation, i.e., Eq. (A11), and the Ornstein-Zernike equation, Eq. (A12), yield a $g_{ii}(r)$ for the ion subsystem. The LFA criterion and the associated hard-sphere approximation can be avoided if desired, by using MD with the pair potential to generate the $g(r)$. The hard-sphere packing fraction η calculated via the LFA criterion is the only parameter extraneous to the KS scheme used in our theory. In calculating the $S(k)$ of complex fluids like carbon, where the leading peak

in $g(r)$ is *not* determined by packing effects but by transient C-C bonding, we use the simple HNC equation.

6. Calculation of the electrical conductivity

The Ziman formula uses the momentum-relaxation-time approximation, while the KG formula typically uses the same approximation when extracting the static conductivity using a Drude fit to the dynamic conductivity $\sigma(\omega)$. The Ziman formula used here is [11]

$$\sigma = 1/R, \quad R = (\hbar/e^2)(3\pi\bar{n}\bar{Z})^{-1}I, \quad (\text{A14})$$

$$I = \int_0^\infty \frac{q^3 \Sigma(q) dq}{1 + \exp\{\beta(\epsilon_q/4 - \mu)\}}, \quad (\text{A15})$$

$$\epsilon_q = (\hbar q^2/2m), \quad \beta = 1/T, \quad (\text{A16})$$

$$\Sigma(a) = S(q)|U_{ei}(q)/2\pi\epsilon(q)|^2, \quad (\text{A17})$$

$$1/\epsilon(q) = 1 + V_q\chi(q, T). \quad (\text{A18})$$

The Born-approximation-like form used here is valid to the same extent that the pseudopotential $U_{ei}(q)$ constructed from the (nonlinear) KS $n_f(r)$ via linear-response theory [Eq. (A7)] is valid. The NPA $S(k)$ is available even for small- k values unlike in DFT-MD simulations where the smallest accessible k value is limited by the finite-size L_{bx} of the simulation cell.

7. Kubo-Greenwood conductivity

The KG dynamic conductivity $\sigma(\omega)$ is a popular approach to determining the static conductivity of WDM systems via DFT-MD simulations [67]. The details of our DFT-MD simulations are given in Sec. II A.

The quenched-crystal KS eigenstates $\phi_\nu(r)$ and eigenvalues ϵ_ν , where ν is a band-index quantum number, are used in the Kubo-Greenwood conductivity as provided in the standard ABINIT code. Usually six to ten such evaluations were obtained by evolving the quenched crystal by further MD simulations (using only the Γ point) and in each case the $\sigma(\omega)$ was obtained [see Fig. 10 for typical aluminum, lithium, and carbon results for $\sigma(\omega)$].

The aluminum $\sigma(\omega)$ is well fitted by the Drude form

$$\sigma(\omega) = \sigma_0/[1 + (\omega\tau)^2], \quad \sigma_0 = \bar{n}\tau. \quad (\text{A19})$$

However, there is no justification for using a Drude form for carbon. The peak position in $\sigma(\omega)$ roughly corresponds to the bonding to antibonding transition in the fluid containing significant covalent bonding [see Fig. 4(b)] at 0.5 eV. This can be seen from the strong peak in $g(r)$ near 3 a.u. (1.55 Å) corresponding to the C-C bond length. This suggests that the $N = 108$ simulation is quite inadequate for complex liquids like carbon, as bonding reduces the effective N of the simulation. In the case of carbon, the static limit of the KG $\sigma(\omega)$ was simply estimated from the trend in the $\omega \rightarrow 0$ region rather than using a Drude fit, but this is an unsatisfactory procedure unless it agrees with the result from, say, the Ziman formula. Furthermore, the different quenched crystals (108 atoms in the simulation) gave significant statistical variations, as reflected in the error bars shown in Fig. 4(a). At higher T , e.g., for $T = 1$ –2 eV, the estimated conductivity behaves

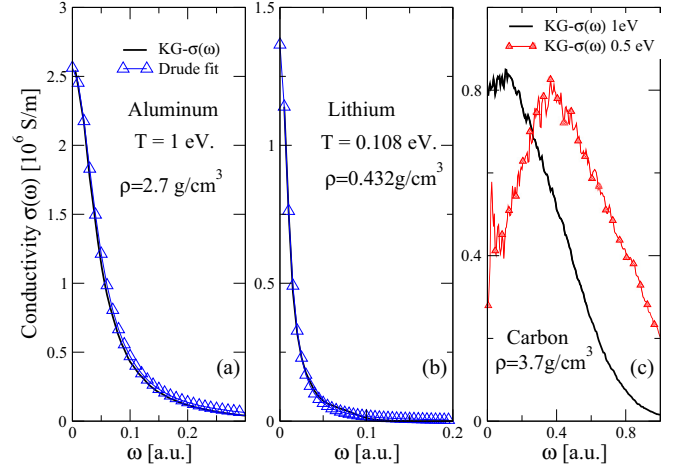


FIG. 10. The KG conductivity $\sigma(\omega)$ for Al, Li, and C. Note the slight non-Drude behavior of Li $\sigma(\omega)$ near 0.08 a.u. in (b). The carbon $\sigma(\omega)$ is highly non-Drude-like, with the peak moving to higher energy as T is lowered; no Drude form is shown for carbon.

similarly to that from the NPA, but somewhat less conductive. The KG formula does not include any self-energy corrections in the one-electron states and excitation energies, and less importantly, no ion-dynamical contributions either, as the ions are stationary (Born-Oppenheimer approximation). The form of $\sigma(\omega)$ including ion dynamics has been discussed by Dharma-wardana in Ref. [68].

8. Conductivity of Li at $T = 4.5$ eV and a density of 0.6 g/cm^3

The conductivity of Li, at density $\rho = 0.6 \text{ g/cm}^3$ at 4.5 eV estimated by Witte *et al.* [43], is roughly a factor of 5 less than that obtained from the NPA-Ziman formula. It is hard to find an explanation for this strong discord, given the good agreement in the XRTS calculation. One possibility is the use of a 64-atom cell in DFT-MD simulations for Li at a chemical potential $\mu \sim 0$. The DFT-MD simulation with the KG formula using $N \sim 100$ atoms in the simulation seems to significantly underestimate σ_0 for low-valence substances like Li and Na, especially as T is increased. Low-valence materials have a small $\mu = E_F$ and hence a modest increase in T can push μ to small values where small- k scattering is important and finally to $\mu < 0$ values (classical regime).

At low T/E_F the major contributions to σ are provided by electron scattering between $-k_F$ and k_F , $k_F = \sqrt{2E_F}$, i.e., momentum changes of the order of $2k_F$. However, at finite T , μ replaces E_F , and as T increases, $\mu \rightarrow 0$ and negative values. The scattering momenta near $\mu \rightarrow +0$ are in the small- k region and involve long-range Coulomb scattering. These contribute significantly to σ at $T = 4.5$ eV for Li at 0.6 g/cm^3 . In Li, if a 64-atom simulation is used, an appropriate length a of the cubic simulation cell would be $a = 20.26$ a.u. The smallest momentum accessible by such a simulation is $\pi/a = 0.16 \text{ (a.u.)}^{-1}$ and hence the corresponding Kubo-Greenwood formula will not sample the small $k < 0.16$ region. We see from Fig. 9 also that the DFT-MD simulations do not provide values for k smaller than $\approx 0.6 \text{ Å}^{-1}$ due to the finite size of the cell used in Ref. [42].

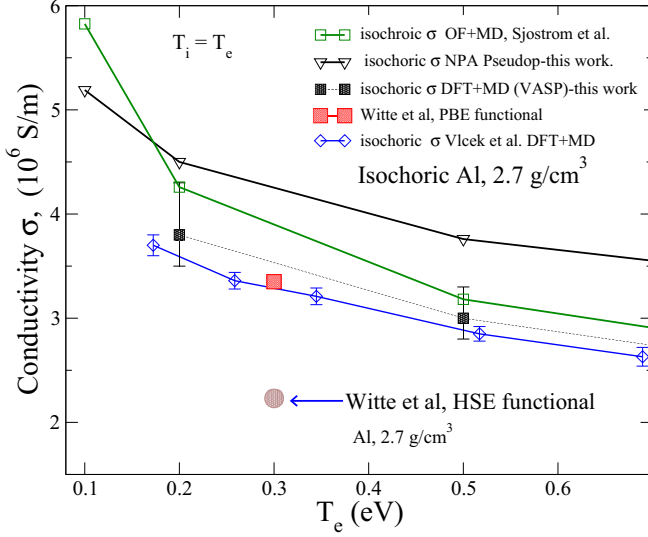


FIG. 11. Isochoric conductivity of aluminum from near its melting point to about 0.7 eV, expanded from Fig. 1, and now including the Witte *et al.* [42] calculation of the Al conductivity at 0.3 eV and $\rho = 2.7 \text{ g/cm}^3$. Our DFT-MD data and those of Vlček *et al.* [35] are shown.

Hence such DFT-MD-KG calculations of σ are strongly weighted to the larger- k strong scattering regime and predict a low conductivity. The results of Pozzo *et al.*, where a 1000-atom simulation was needed for Na, is a case in point. However, such large simulations are beyond the scope of most laboratories, while NPA-type approaches usually provide good results in all cases that we have studied.

9. Isobaric and isochoric conductivity of aluminum in the liquid-metal region

High-quality experimental data (errors of $\pm 6\%$) are available for the isobaric conductivity σ_{ib} of liquid aluminum at low T [15,16]. The relevant region, viz., (a) of Fig. 1, is shown enlarged to display the experimental and calculated data in Fig. 2. The NPA calculation is in excellent agreement with the experiment of Gathers, to well within the error bars. On the other hand, the DFT-MD calculation captures about 75% of the experimental conductivity. An ~ 100 -atom simulation cannot capture the k values smaller than $\pi/a \sim 0.12 \text{ (a.u.)}^{-1}$ for Al at this density, and may contribute to some of the underestimate.

Isochoric conductivities (with $\rho = 2.7 \text{ g/cm}^3$) of aluminum obtained from the NPA calculation and from the DFT-MD calculation by us and by Vlček *et al.* [35] are shown in Fig. 11, together with a single data point from Witte *et al.* [42] with the PBE functional and also with the HSE functional. The result obtained using the HSE XC functional is a strong underestimate compared to other DFT-MD [50,69], orbital-free [33], and NPA estimates.

In Ref. [42] Witte *et al.* strongly argue for the HSE functional even for aluminum, a simple metal proven to work well with more standard approaches, and propose that there are strong electron-electron interactions in Al. The value of $2.23 \times 10^6 \text{ S/m}$ quoted by them at 0.3 eV, 2.7 g/cm^3 , is taken

to agree with experiment, based on their interpretation of the experimental data of Gathers [15]. However, as discussed below, Gathers' datum at 0.3 eV ($\approx 3500 \text{ K}$) is for isobaric aluminum at $\rho = 1.875 \text{ g/cm}^3$ and 0.3 GPa and the Witte *et al.* interpretation is incorrect.

10. Experimental data of Gathers

Gathers measures the resistivity of aluminum in an isobaric experiment, starting from the solid ($\rho_0 = 2.7 \text{ g/cm}^3$ and $v_0 = 0.37 \text{ cm}^3/\text{g}$) and heating to the range 933–4000 K at 0.3 GPa [15]. Gathers himself recommends the Gol'tsova-Wilson [70,71] volume expansion data rather than those measured by him. In Table II of Ref. [15], the experimental resistivity (raw data) calculated using the nominal enthalpy input to the sample is given in column 5. The apparatus and the sample undergo volume expansion; the resistivities for the input enthalpy corresponding to the volume expanded sample (using the Gol'tsova-Wilson data) are given in column 4 of the same table. Hence the volume-corrected isobaric resistivity for aluminum in the range ($T = 993 \text{ K}, \rho = 2.42 \text{ g/cm}^3$) to ($T = 4000 \text{ K}, \rho = 1.77 \text{ g/cm}^3$) are the values found in column 4, while column 5 gives the raw data. Column 4 resistivities agree with the isobaric resistivity values that may also be obtained from the fit formula given in the last row of Table 23 of [16].

Since Table II given by Gathers is somewhat misleading, we have recalculated the resistivities R (see Table I) using the fit equations given by Gathers. His Eq. (8) in [15] gives the (expansion-uncorrected) raw data, labeled R_G . The expansion correction essentially brings the input heat to the actual volume of the sample. Thus Eq. (9) in [15], where the enthalpy input is corrected for volume expansion, agrees with Gathers' fit equation given subsequently in Ref. [16] and hence labeled $R_{[16]}$. Gathers uses the enthalpy as the primary variable in Eqs. (8) and (9) of [15], but also gives R_G directly as a function of v/v_0 in Eq. (10) of [15]. Thus Eqs. (8) and (10) of [15] yield the same resistivity R_G at a given density and corresponding T , while Eq. (9) of [15] is the volume-corrected equation restated in the review in Ref. [16].

According to Gathers, the experimental resistivities have an error of $\sim \pm 6\%$. The relevant equations from Gathers' work in [15] are given below:

$$H = 0.0048910 + 0.0010704T + 2.3084 \times 10^{-8} T^2 \quad [\text{Gathers' Eq. (6)}], \quad (\text{A20})$$

$$v/v_0 = 1.0205 + 8.3779 \times 10^{-2} H + 4.9050 \times 10^{-3} H^2 \quad [\text{Gathers' Eq. (7)}], \quad (\text{A21})$$

$$R_9 = 0.1494 + 7.9448 \times 10^{-2} H - 1.3189 \times 10^{-3} H^2 \quad [\text{Gathers' Eq. (9)}], \quad (\text{A22})$$

$$1.12 \leq v/v_0 \leq 1.56 \quad (\text{i.e., } 2.411 \text{ g/cm}^3 \leq \text{density} \leq 1.731 \text{ g/cm}^3). \quad (\text{A23})$$

The enthalpy H can be eliminated in Gathers' Eq. (9), i.e., (A22), using the preceding equations. The result agrees with the fit equation given in the subsequent review article by

Gathers [16], Table 23 (last row). This is given as a fit for the isobaric resistivity (at 0.3 GPa) ($\mu\Omega\text{ m}$), viz.,

$$R(v) = -1.0742 + 4.1997 \times 10^3 v - 2.5124 \times 10^6 v^2. \quad (\text{A24})$$

Here v is the volume in $\text{m}^3 \text{kg}^{-1}$ with $4.1 \times 10^{-5} \leq v \leq 5.78 \times 10^{-4}$. The resistivity calculated from this equation agrees with column 4 of Table II of Gathers [15].

The NPA calculation that takes the nuclear charge, temperature, and density as the basic inputs and uses the finite- T PDW XC functional (LDA) [47] gives excellent agreement for σ_{ib} with the Gathers data at all densities listed in Table I, as shown in Fig. 2. At $T = 0.3 \text{ eV}$, $\rho = 1.875 \text{ g/cm}^3$ and $\sigma_{\text{ib}} = 2.22 \times 10^6 \text{ S/m}$, while the HSE functional used

with MD-DFT-KG formula gives this conductivity only at 2.7 g/cm^3 , as reported by Witte *et al.* [42].

Our DFT-MD estimates of the isochoric conductivity using the PBE functional, the DFT-MD estimates of Vlček *et al.*, and the Witte *et al.* DFT-MD estimate [42] using the PBE functional for 2.7 g/cm^3 at 0.3 eV are in close agreement. They all fall below the NPA-Ziman estimate and we attribute this partly to the inability of the DFT-MD-KG approach to access small- k scattering contributions unless the number of atoms N in the simulation is sufficiently large. Furthermore, as $T/E_F \rightarrow 0$, the estimate of the derivative of the Fermi function and also the matrix element of the velocity operator probably require an increasingly dense mesh of k points.

-
- [1] A. Ng, *Int. J. Quantum Chem.* **112**, 150 (2012).
 - [2] H. M. Milchberg, R. R. Freeman, S. C. Davey, and R. M. More, *Phys. Rev. Lett.* **61**, 2364 (1988).
 - [3] M. W. C. Dharma-wardana, *Solid State Commun.* **86**, 83 (1993).
 - [4] S. Vaziri, G. Lupina, C. Henkel, A. D. Smith, M. Östling, J. Dabrowski, G. Lippert, W. Mehr, and M. C. Lemme, *Nano Lett.* **13**, 1435 (2013).
 - [5] N. Medvedev, U. Zastrau, E. Förster, D. O. Gericke, and B. Rethfeld, *Phys. Rev. Lett.* **107**, 165003 (2011).
 - [6] L. Harbour, M. W. C. Dharma-wardana, D. D. Klug, and L. J. Lewis, *Phys. Rev. E* **95**, 043201 (2017).
 - [7] M. Pozzo, M. P. Desjarlais, and D. Alfè, *Phys. Rev. B* **84**, 054203 (2011).
 - [8] S. Sinha, P. L. Srivastava, and R. N. Singh, *J. Phys.: Condens. Matter* **1**, 1695 (1989).
 - [9] I. Tamblyn, J.-Y. Raty, and S. A. Bonev, *Phys. Rev. Lett.* **101**, 075703 (2008).
 - [10] M. W. C. Dharma-wardana, *Contrib. Plasma Phys.* **55**, 85 (2015).
 - [11] F. Perrot and M. W. C. Dharma-wardana, *Phys. Rev. E* **52**, 5352 (1995).
 - [12] F. Perrot, *Phys. Rev. E* **47**, 570 (1993).
 - [13] G. Kresse and J. Furthmüller, *Phys. Rev. B* **54**, 11169 (1996).
 - [14] X. Gonze and C. Lee, *Comput. Phys. Commun.* **180**, 2582 (2009).
 - [15] G. R. Gathers, *Int. J. Thermophys.* **4**, 209 (1983).
 - [16] G. K. Gathers, *Rep. Prog. Phys.* **49**, 341 (1986).
 - [17] R. K. Williams, G. L. Coleman, and D. W. Yarbrough, Oak Ridge National Laboratory Report No. ORNL/TM-10622, 1988.
 - [18] D. Kraus, J. Vorberger, D. O. Gericke, V. Bagnoud, A. Blazevic, W. Cayzac, A. Frank, G. Gregori, A. Ortner, A. Otten, F. Roth, G. Schaumann, D. Schumacher, K. Siegenthaler, F. Wagner, K. Wunsch, and M. Roth, *Phys. Rev. Lett.* **111**, 255501 (2013).
 - [19] H. D. Whitley, D. M. Sanchez, S. Hamel, A. A. Correa, and L. X. Benedict, *Contrib. Plasma Phys.* **55**, 390 (2015).
 - [20] M. W. C. Dharma-wardana, *arXiv:1707.08880*.
 - [21] V. Recoules, J. Clerouin, G. Zerah, P. M. Anglade, and S. Mazevet, *Phys. Rev. Lett.* **96**, 055503 (2006).
 - [22] D. Li, D. Li, H. Liu, S. Zeng, C. Wang, Z. Wu, P. Zhang, and J. Yan, *Sci. Rep.* **4**, 5898 (2014).
 - [23] H. C. Chen and S. K. Lai, *Phys. Rev. A* **45**, 3831 (1992).
 - [24] N. H. March, *Can. J. Phys.* **65**, 219 (1987).
 - [25] A. P. Lyubartsev and A. Laaksonen, *Phys. Rev. E* **52**, 3730 (1995).
 - [26] M. W. C. Dharma-wardana and F. Perrot, *Phys. Rev. A* **26**, 2096 (1982).
 - [27] M. S. Murillo, J. Weisheit, S. B. Hansen, and M. W. C. Dharma-wardana, *Phys. Rev. E* **87**, 063113 (2013).
 - [28] T. Blenski, R. Piron, C. Caizergues, and B. Cichocki, *High Energy Density Phys.* **9**, 687 (2013).
 - [29] J. F. Benage, W. R. Shanahan, and M. S. Murillo, *Phys. Rev. Lett.* **83**, 2953 (1999).
 - [30] M. W. C. Dharma-wardana, *Phys. Rev. E* **73**, 036401 (2006).
 - [31] H. Reinholz, R. Redmer, G. Röpke, and A. Wierling, *Phys. Rev. E* **62**, 5648 (2000).
 - [32] P. Sperling, E. J. Gamboa, H. J. Lee, H. K. Chung, E. Galtier, Y. Omarbakiyeva, H. Reinholz, G. Röpke, U. Zastrau, J. Hastings, L. B. Fletcher, and S. H. Glenzer, *Phys. Rev. Lett.* **115**, 115001 (2015).
 - [33] T. Sjostrom and J. Daligault, *Phys. Rev. E* **92**, 063304 (2015).
 - [34] The experimental value is quoted in C. R. Leavens, A. H. MacDonald, R. Taylor, A. Ferraz, and N. H. March, *Phys. Chem. Liq.* **11**, 115 (1981).
 - [35] V. Vlček, N. de Koker, and G. Steinle-Neumann, *Phys. Rev. B* **85**, 184201 (2012).
 - [36] M. W. C. Dharma-wardana, *Phys. Rev. E* **93**, 063205 (2016).
 - [37] J. P. Perdew, K. Burke, and M. Ernzerhof, *Phys. Rev. Lett.* **77**, 3865 (1996).
 - [38] M. W. C. Dharma-wardana and F. Perrot, *Phys. Lett. A* **163**, 223 (1992).
 - [39] G. Faussurier and C. Blancard, *Phys. Rev. E* **91**, 013105 (2015).
 - [40] F. Perrot and M. W. C. Dharma-wardana, *Int. J. Thermophys.* **20**, 1299 (1999).
 - [41] J. K. Yuan, Y. S. Sun, and S. T. Zheng, *Phys. Rev. E* **53**, 1059 (1996).
 - [42] B. B. L. Witte, L. B. Fletcher, E. Galtier, E. Gamboa, H. J. Lee, U. Zastrau, R. Redmer, S. H. Glenzer, and P. Sperling, *Phys. Rev. Lett.* **118**, 225001 (2017). We have communicated with the authors regarding their value of the Li conductivity [43], as well as the aluminum conductivity given in Ref. [42]; see the review of Gathers' experimental data given in the Appendix ensuing from our discussions.
 - [43] B. B. L. Witte, M. Shihab, S. H. Glenzer, and R. Redmer, *Phys. Rev. B* **95**, 144105 (2017).
 - [44] J. Heyd, G. E. Scuseria, and M. Ernzerhof, *J. Chem. Phys.* **118**, 8207 (2003).

- [45] R. Redmer, S. Glenzer, B. Witte, P. Sperling, G. Röpke, and H. Reinholz (private communication).
- [46] A. Kietzmann, R. Redmer, M. P. Desjarlais, and T. R. Mattsson, *Phys. Rev. Lett.* **101**, 070401 (2008).
- [47] F. Perrot and M. W. C. Dharma-wardana, *Phys. Rev. B* **62**, 16536 (2000); **67**, 079901(E) (2003); [arXiv:1602.04734](https://arxiv.org/abs/1602.04734).
- [48] M. W. C. Dharma-wardana, *Computation* **4**, 16 (2016).
- [49] M. W. C. Dharma-wardana and R. Taylor, *J. Phys. C* **14**, 629 (1981).
- [50] M. P. Desjarlais, J. D. Kress, and L. A. Collins, *Phys. Rev. E* **66**, 025401(R) (2002).
- [51] D. Alfè (private communication).
- [52] B. Darwent, *Bond Dissociation Energies in Simple Molecules*, Natl. Bur. Stand. Ref. Data Ser, Natl. Bur. Stand. (US) Circ. No. 31, (US GPO, Washington, DC, 1970); http://www.wiredchemist.com/chemistry/data/bond_energies_lengths.htm
- [53] M. W. C. Dharma-wardana and F. Perrot, *Phys. Rev. Lett.* **65**, 76 (1990).
- [54] K. P. Driver and B. Militzer, *Phys. Rev. Lett.* **108**, 115502 (2012).
- [55] L. Harbour, M. W. C. Dharma-wardana, D. D. Klug, and L. J. Lewis, *Phys. Rev. E* **94**, 053211 (2016).
- [56] P. A. Sterne, S. B. Hansen, B. G. Wilson, and W. A. Isaacs, *High Energy Density Phys.* **3**, 278 (2007).
- [57] C. Dharma-wardana and F. Perrot, in *Density Functional Theory*, edited by E. K. U. Gross and R. M. Dreizler, NATO Advanced Studies Institute, Series B: Physics (Plenum, New York, 1993), Vol. 337, p. 625.
- [58] F. Perrot and M. W. C. Dharma-wardana, *Phys. Rev. A* **29**, 1378 (1984).
- [59] F. Perrot, Y. Furutani, and M. W. C. Dharma-wardana, *Phys. Rev. A* **41**, 1096 (1990).
- [60] R. Piron and T. Blenski, *Phys. Rev. E* **83**, 026403 (2011).
- [61] M. W. C. Dharma-wardana, *A Physicist's View of Matter and Mind* (World Scientific, Hackensack, 2013), Chaps. 8 and 9.
- [62] S. H. Glenzer and R. Redmer, *Rev. Mod. Phys.* **81**, 1625 (2009).
- [63] C. E. Starrett and D. Saumon, *Phys. Rev. E* **87**, 013104 (2013).
- [64] C. E. Starrett, D. Saumon, J. Daligault, and S. Hamel, *Phys. Rev. E* **90**, 033110 (2014).
- [65] M. W. C. Dharma-wardana, [arXiv:1707.08880](https://arxiv.org/abs/1707.08880).
- [66] F. Lado, S. M. Foiles, and N. W. Ashcroft, *Phys. Rev. A* **28**, 2374 (1983).
- [67] V. Recoules, P. Renaudin, J. Cléroutin, P. Noiret, and G. Zérah, *Phys. Rev. E* **66**, 056412 (2002).
- [68] M. W. C. Dharma-wardana, in *Laser Interactions with Atoms, Solids, and Plasmas*, edited by R. M. More (Plenum, New York, 1994), p. 311.
- [69] V. Recoules and J. P. Crocombette, *Phys. Rev. B* **72**, 104202 (2005).
- [70] E. J. Gol'tsova, *High Temp. (USSR)* **3**, 438 (1965).
- [71] R. P. Wilson, Jr., *High Temp. Sci.* **1**, 367 (1969).